Front. Struct. Civ. Eng.
DOI 10.1007/s11709-017-0384-z

RESEARCH ARTICLE

Probabilistic safety assessment of self-centering steel braced frame

Navid RAHGOZAR[a,*], Nima RAHGOZAR[a], Abdolreza S. MOGHADAM[b]

[a] *Department of Structural Engineering, Science and Research Branch, Islamic Azad University, Tehran, Iran*
[b] *Structural Engineering Research Center, International Institute of Earthquake Engineering and Seismology (IIEES), Tehran, Iran*
[*] *Corresponding author. E-mail: n.rahgozar@srbiau.ac.ir*

ABSTRACT The main drawback of conventional braced frames is implicitly accepting structural damage under the design earthquake load, which leads to considerable economic losses. Controlled rocking self-centering system as a modern low-damage system is capable of minimizing the drawbacks of conventional braced frames. This paper quantifies main limit states and investigates the seismic performance of self-centering braced frame using a Probabilistic Safety Assessment procedure. Margin of safety, confidence level, and mean annual frequency of the self-centering archetypes for their main limit states, including PT yield, fuse fracture, and global collapse, are established and are compared with their acceptance criteria. Considering incorporating aleatory and epistemic uncertainties, the efficiency of the system is examined. Results of the investigation indicate that the design of low- and mid-rise self-centering archetypes could provide the adequate margin of safety against exceeding the undesirable limit-states.

KEYWORDS self-centering steel braced frame, mean annual frequency, safety assessment, confidence level, margin of safety

1 Introduction

Main building codes [1,2] ensure life-safety and collapse prevention of conventional buildings under design earthquake loads using ductility and strength capacity of members [3]. However, code-compliant buildings incur significant damage during a severe earthquake [4]. Nowadays, the new generation of lateral resisting systems such as rocking braced steel frames [5], rocking wall-frame structures [6,7], self-centering timber systems [8,9], confined masonry rocking walls [10], and post-tensioned steel moment resisting frames [11,12] have been developed to overcome technical flaws and socio-economic drawbacks of conventional buildings. Previous studies have shown that these low-damage systems can significantly reduce soft-story failure, drift concentration, and plastic deformation of structural elements by directing damages to replaceable energy dissipation devices such as steel yielding fuses [13,14], viscous dampers [15], and friction bearings [16].

Unlike conventional fixed-based system, the self-centering system is isolated from gravity framing system, which makes it possible to rock upon the foundation during an earthquake. The pioneering efforts to examine the efficiency of self-centering systems are due to Clough and Huckelbridge [17] and Kelley and Tsztoo [18] studies, and, more recently, it has been confirmed for several types of self-centering systems [19–21]. There are several configurations for self-centering systems equipped with different fuse types and post-tensioning locations. A number of studies have focused on performance of the single [14–16] and dual configuration controlled-rocking frame equipped with PT strands and different energy dissipation devices. The post-tensioning strands are restrained uprightly to the top and bottom of the frames and yielding fuses are placed between two rocking frames. Post-tensioning strands provide restoring forces and prevent permanent displacement and replaceable fuses are to damp the seismic energy. A team from Lehigh University was the pioneering researchers to explore the self-centering chevron-braced frames (0.6-scale) equipped with friction-bearing dampers [22], which was tested using multi-dimensional hybrid simulations [23]. The simplified analytical method for estimating structural demands of this system were

Article history: Received Aug 23, 2016; Accepted Oct. 20, 2016

proposed by Roke et al. [16] and further analytical studies have been done by Sause et al. [24] and Chancellor et al. [25]. Working in collaboration with researchers at the University of Illinois, Ma et al. [14] tested the three-story single self-centering frame (0.68-scale) on the E-defense shaking table. As another alternative configuration of self-centering systems, Wiebe and Christopoulos [27] tested the 8-story multiple rocking joints self-centering systems (0.3-scale) to mitigate the deficiency of higher mode effects and proposed a performance based design strategy [3]. The examples of self-centering systems were also implemented in practice [15,28].

This paper investigates the performance of dual configuration of the self-centering brace frame equipped with yielding fuses and post-tensioning strands (Fig. 1(a)). This system was developed by researchers at the University of Illinois at Urbana-Champaign. Eatherton et al. [26] conducted the quasi-static cyclic tests (0.43-scale) of rocking frames. Eatherton and Hajjar [13] performed the similar system equipped with different combinations of fuses and post-tensioning. Rahgozar et al. [29] have also quantified the seismic performance factors of self-centering special concentrically braced frames. This paper aims to quantify main limit states and investigates the safety assessment of dual configuration self-centering braced frames, which are designed based on the previous studies.

Figure 1(b) shows the push-over curve and an ideal hysteretic behavior of the dual configuration self-centering braced frame, which minimizes the structural damage with its flag-shaped behavior. The hysteresis (Fig. 1(b)) composed of PT strands and fuses behaviors has three main branches: the first branch (K_{OA}) shows elastic behavior of the system that terminates when it initiates to rock (point A; corresponding to the uplift strength (V_{up}) and uplift drift (δ_{up}) values); then, there is a hardening branch with the stiffness of K_{AB} to the system yielding point (point B; corresponding to yield strength (V_y) and yield drift (δ_y) values). The yielding strength point of the system is the beginning of the post-yield hardening branch with the hardening ratio of α. The system dissipates seismic energy using energy dissipation devices during unloading phase.

In spite of the extensive research efforts, only a few probabilistic studies have been reported to assess the safety of self-centering systems under the high seismic intensities. Studies on self-centering steel moment resisting frame [30], self-centering braced frame with friction damper [31], and yielding fuses [26] are only those that have been conducted on their collapse assessment analysis. This paper determines the probabilistic seismic performance of self-centering systems and quantifies limit states and seismic behavior through Probabilistic Safety Assessment (PSA) procedure. According to Fig. 2, in the following parts of this paper, through probabilistic analysis the safety of designed self-centering archetypes is examined. To obtain analysis requirements including quantified limit-states, performance levels, fractile IDAs, epistemic dispersion, and fragility curves, the selected archetypes are simulated and then analyzed. Finally, using the mean annual frequency (MAF), safety margin ratio, and confidence level measures, the safety of self-centering archetypes are investigated from various aspects.

According to Fig. 2, in the following parts of this paper, through probabilistic analysis the safety of designed self-centering archetypes is examined. To obtain analysis requirements including quantified limit-states, performance levels, fractile IDAs, epistemic dispersion, and fragility curves, the selected archetypes are simulated and then analyzed. Finally, using the mean annual frequency (MAF), safety margin ratio, and confidence level mea-

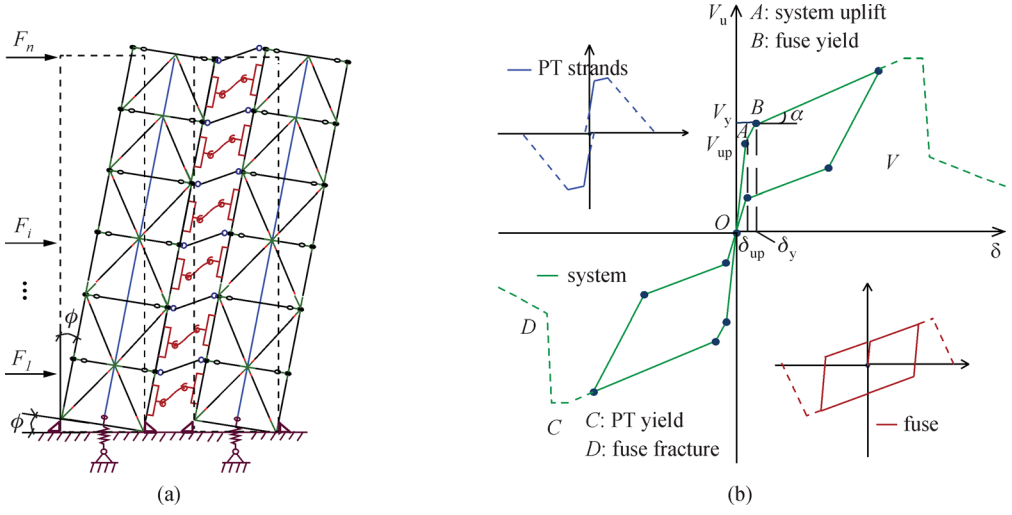

Fig. 1 (a) Configuration of the self-centering system; (b) push and hysteretic curves of the self-centering system, fuse and PT strand components

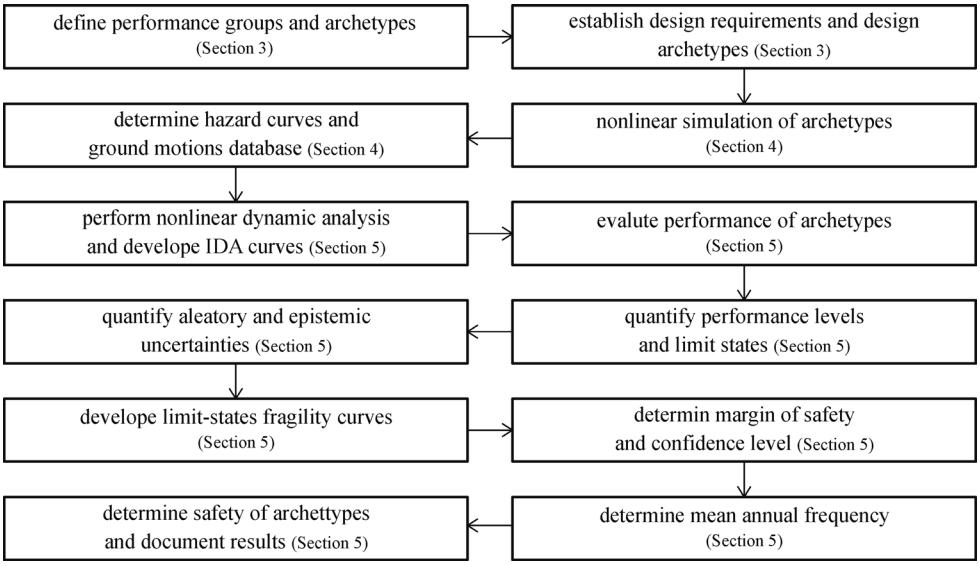

Fig. 2 Outline procedure for PSA of the self-centering steel braced frame

sures, the safety of self-centering archetypes are investigated from various aspects.

2 Probabilistic safety assessment

In the absence of seismic uncertainty, the structural-safety of a building could be simply examined from static analysis through comparing structural demands with the capacity of members. However, the structural seismic demands are probabilistic inherently, related to earthquakes uncertainties. The probabilistic approaches provide a reliable method for safety checking of the structure under uncertainties [32]. SAC/FEMA [33] and Performance-Based Earthquake Engineering (PBEE) frameworks provide reliable probabilistic techniques for seismic assessment and designing of the buildings. These methodologies use Probabilistic Safety Assessment (PSA) to determine Confidence Level (CL) and Mean Annual Frequency (MAF) of exceedance of engineering demand parameters for a specific building located in seismic site region. Using PSA, safety of the structure, by considering incorporating aleatory and epistemic uncertainties, can be easily assessed. The aleatory uncertainty is due to the natural randomness of earthquakes and the epistemic variability is the scientific uncertainty in the model arises from the limited data and lack of knowledge. In general, PSA approach presents a probabilistic closed-form solution to solve the following safety equation:

$$\lambda_{EDP}^{LS}(\mathrm{edp}) \leqslant \lambda^{P_0} \tag{1}$$

where λ_{EDP}^{LS}, is the MAF of exceedance of an Engineering Demand Parameter (edp) for a given limit state and λ^{P_0} denotes an acceptable risk of occurring a limit state at a given seismic intensity, which is a mean sense of MAF value.

According to PSA, the MAF of exceeding an edp for the given a limit-state, λ_{EDP}^{LS}, can be calculated by integration the conditional probability of structure demands over all possible levels of seismic intensity, which can be shown mathematically as follows [34]:

$$\lambda_{EDP}^{LS}(edp) = \int_0^{\infty} P(EDP > edp^{LS} | IM = im) \left| \frac{\mathrm{d}\lambda_{IM}(im)}{\mathrm{d}(im)} \right| \mathrm{d}(im) \leqslant \lambda^{P_0}, \tag{2}$$

where EDP and edp^{LS} are abbreviations of the engineering demand parameter (e.g., roof drift and inter-story drift) and specified limit of EDP for the desired limit-state. IM denotes a ground motion intensity measure (e.g., PGA and $Sa(T_1)$) and $P(EDP > edp^{LS}|IM = im)$ is a conditional probability exceedance of a given edp for a specified limit state (limit state fragility curve), which can be computed from incremental dynamic analysis, (IDA). In addition, the term of $\lambda_{IM}(im)$ refers to the hazard curve, which is equal to the mean annual frequency of IM that is exceeding a specified im level, and $\left| \frac{\mathrm{d}\lambda_{IM}(im)}{\mathrm{d}(im)} \right| \mathrm{d}(im)$ is an absolute value of the derivative of a hazard curve at intensity im. Note that safety of the building satisfies when the MAF of exceedance of the limit state, λ_{EDP}^{LS}, becomes lower than acceptance measure of λ^{P_0}.

The value of λ_{EDP}^{LS} could be computed by numerical integration of the probability of demands over all possible levels of ground motion intensity. However, among the proposed methods for estimation of λ_{EDP}^{LS} [35–38], SAC/FEMA presents a closed-form solution considering a series

of assumptions to simplify calculations. Figure 3 shows the schematic plan of SAC/FEMA methodology. Figure 3(a) shows the hazard curves, $\lambda_{IM}(im)$, which is the annual probability of exceeding intensity level of IM, $P[IM > im]$, and mentions a sample of IDA results along with 50%, 16% and 84% fractile IDAs as the median lower and upper bounds of results. Considering assumptions to fit the seismic hazard curve ($\lambda_{IM}(im)$; Fig. 3(a)) of a building site and estimating the median of IDA results, the following equation is established to approximate the λ_{EDP}^{LS} [36]:

$$\lambda_{EDP}^{LS} = H\left[\left(\frac{\hat{c}}{a}\right)^{\frac{1}{b}}\right] \times \exp\left[\frac{1}{2}\frac{k^2}{b^2}\left(\beta_{EDP,R|IM}^2 + \beta_C^2\right)\right], \quad (3)$$

where $\hat{c}$ is a median capacity of the structure and β_C is the dispersion of $\hat{c}$ (Fig. 3(b)). $\beta_{EDP,R|IM}$ is the inherent aleatory randomness of demand (Record-to-record uncertainties) obtained from IDAs at each intensity level (Fig. 3(b)). Parameters of a, b, k, and k_0 are the constant values for predicting the median IDA curve, $\hat{EDP}(IM)$, and hazard curves, $\lambda_{IM}(im)$, using power-law function as follows [39]:

$$\hat{EDP}(IM) \approx a \times (IM)^b, \quad (4)$$

$$\lambda_{IM}(im) = k_0(IM)^{-k} = k_0 \times \exp\left(-k \times \ln(IM)\right). \quad (5)$$

By rearranging Eq. (3), confidence level, X, of the structure in satisfying a given performance objective can be defined from its standard normal value of inverse cumulative distribution index by the following equations:

$$K_X = \Phi_X^{-1} = \frac{\left[-\ln(\lambda_X) + \frac{1}{2}\frac{k}{b}\beta_{\text{total},U}^2\right]}{\beta_{\text{total},U}}. \quad (6)$$

In which λ_X is:

$$\lambda_X = \frac{\gamma \times \hat{EDP}}{\varphi \times \hat{C}} = \exp\left[-\beta_{\text{total},U}\left(K_{C_L} - \frac{1}{2}\frac{k}{b}\beta_{\text{total},U}\right)\right], \quad (7)$$

$$\phi = \exp\left[-\frac{1}{2}\frac{k}{b}\left(\beta_{C,R}^2 + \beta_{C,U}^2\right)\right],$$

$$\gamma = \exp\left[-\frac{1}{2}\frac{k}{b}\left(\beta_{EDP,R}^2 + \beta_{EDP,U}^2\right)\right],$$

where $\beta_{EDP,U}$ and $\beta_{C,U}$ are the demand and capacity uncertainties and $\beta_{\text{total},U} = \sqrt{\left(\beta_{C,U}^2 + \beta_{EDP,U}^2\right)}$ is an SRSS of the total epistemic uncertainty. $\beta_{C,R}$ and $\beta_{EDP,R}$ are the aleatory randomness of structural capacity and demand parameters.

3 Studied archetypes

A set of design assumptions such as number of stories, relative-span ratio (A/B, where A is frame width and B is the span between two adjacent frames), number of self-centering frame in each direction of the building, and self-centering ratio (SC: denotes the ratio of the uplift moment to the yield moment of the fuse) is chosen to reduce the design space of controlled rocking archetypes. In general, 12 archetypes with various building height (3-, 6-, and 9-story), seismic frame type (space/perimeter), condition of gravity load level, and seismic design categories (SDC $D_{\max}$ and $D_{\min}$), are categorized into four performance groups (PGs), as summarized in Table 1. The typical samples of the plans and elevations for space and perimeter archetypes are shown in Fig. 4. In each direction of the 6/9-

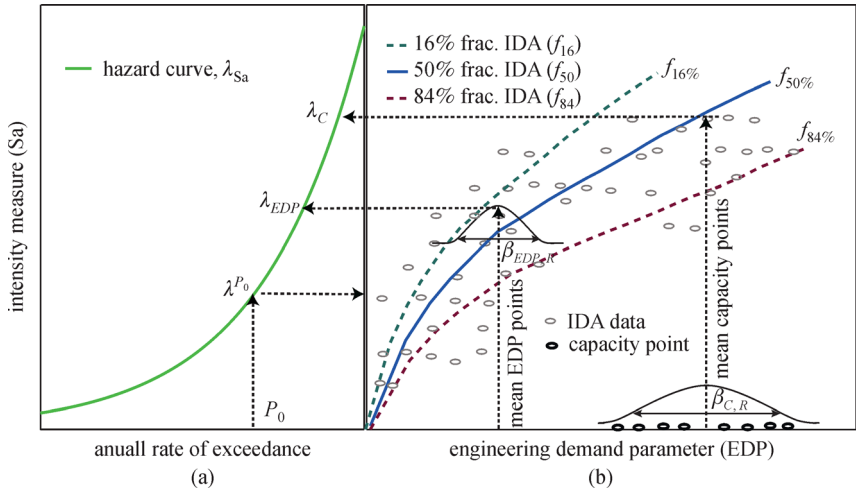

Fig. 3 Schematic plan of the PSA procedure: correlation between (a) seismic hazard curve and (b) structural demand and capacity parameters

Table 1 Performance groups along with considered archetypes

performance		archetype stories	number of archetype in each direction	design load level		
group ID	design ID			gravity frame type	seismic loads	seismic design category
	A_1	3	2	perimeter	low	D_{max}
PG_1	A_2	6	4	perimeter	low	D_{max}
	A_3	9	4	perimeter	low	D_{max}
	A_4	3	2	perimeter	low	D_{max}
PG_2	A_5	6	4	perimeter	low	D_{max}
	A_6	9	4	perimeter	low	D_{max}
	A_7	3	2	space	high	D_{max}
PG_3	A_8	6	4	space	high	D_{max}
	A_9	9	4	space	high	D_{max}
	A_{10}	3	2	space	high	D_{max}
PG_4	A_{11}	6	4	space	high	D_{max}
	A_{12}	9	4	space	high	D_{max}

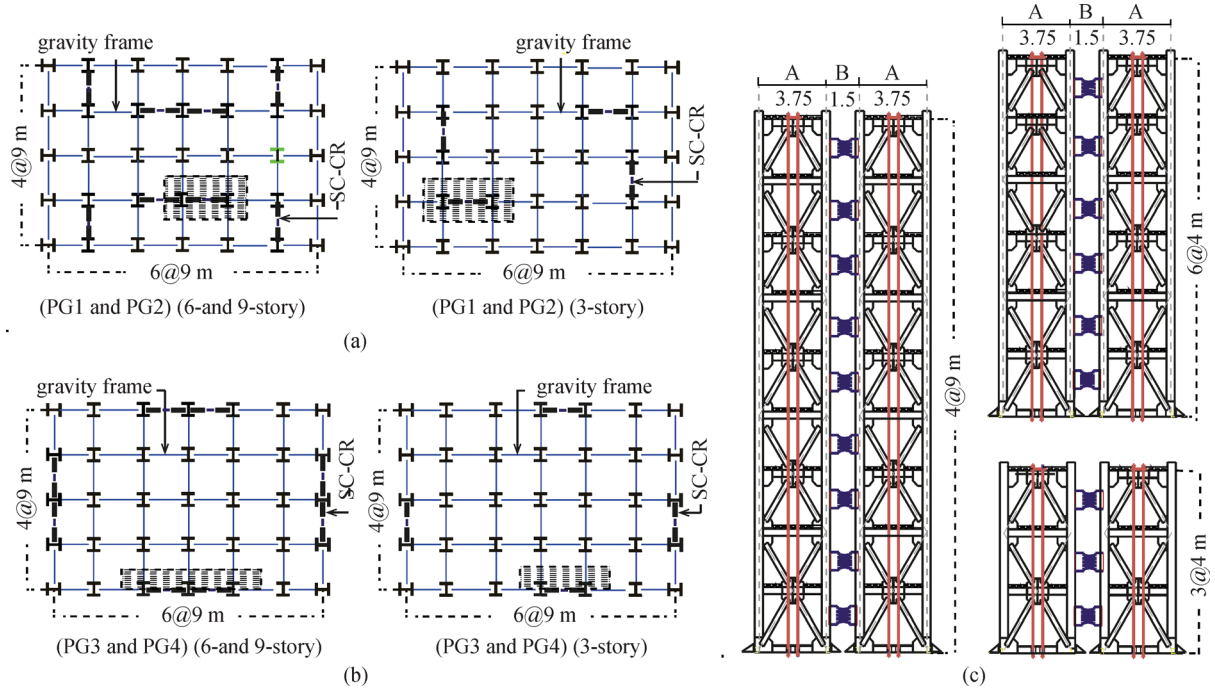

Fig. 4 Configurations of self-centering braced frame archetypes. (a) space SC-CR; (b) perimeter SC-CR; (c) perimeter and space SC-CR

story and 3-story buildings, four and two seismic archetypes are used (Figs. 4(a) and 4(b)), respectively. Story height and spanning ratio (A/B) are equal to 4 m and 2.5, respectively.

The archetypes are assumed to be located in Los Angeles, California, designated with a seismic design category D. The spectral response acceleration parameters of SD_1 = 1 g and SD_s = 0.6 g for archetypes assigned at SDC D_{max} (high seismic region) and SD_1 = 0.49 g and SD_s = 0.19 g for archetypes at SDC D_{min} (low seismicity region) are taken for designed archetypes in accordance with ASCE7-10 [1].

The archetypes are designed by a limit states methodology proposed by Eatherton et al. [40]. The required overturning strengths (M_u) of the archetype are determined using equivalent lateral force procedure with response modification factor of R = 8 [31]. To design the archetypes components, the required initial post-tensioning force (F_{PTi}) and shear strength of fuse (V_{fp}) are determined by the following Eqs. [13]:

$$F_{PTi} \geqslant \frac{M_u}{\phi(1+SC)}\frac{SC}{A} - 0.9P_{\mathrm{D}}, \quad (8)$$

$$V_{fp} \geqslant \frac{Mu}{\phi(1+SC)(A+B)}, \quad (9)$$

where P_{D} is the attributed gravity load to the archetype and ϕ is the strength reduction factor.

Figure 5 shows the configuration and material behavior of the post-tensioning strand and shear plate of the fuse. High strength post-tensioning strands with 7 individual woven wires with the nominal diameter of 15.9 mm, are designed by the following equations:

$$A_{PT} = \frac{F_{pti}}{\left(\varepsilon_{\mathrm{target}} - \frac{A \times RDR_{\mathrm{target}}}{2L_{PT}}\right)E_{PT}}; \varepsilon_{\mathrm{target}} < \varepsilon_{\mathrm{limit}}, \quad (10)$$

where A_{PT} is a required cross-sectional area of PT strands, E_{PT} and L_{PT} are the modulus of elasticity and length of post-tensioning strands. $\varepsilon_{\mathrm{target}}$ denotes a combination of an initial PT strain (ε_{i}) due to F_{pti} and an applied strain at the given target roof drift ratio, RDR_{target}. $\varepsilon_{\mathrm{limit}}$ is the PT strain limit and depends on the material type and anchorage system of PT cables [40].

The replaceable butterfly-shaped fuses, known as ductile energy dissipation devices with stable hysteretic behavior, are designed by Ref. [41]:

$$N_{fs} \cdot Nl_{fs} = \frac{9}{4}\frac{V_{fp}}{f_{yfs}}\frac{L_{fs}}{b_{fs}^2 t_{fs}}, \quad (11)$$

where N_{fs} and Nl_{fs} denote the required number of fuses and the number of links per fuse. L_{fs}, b_{fs}, t_{fs}, and fy_{fs} are the effective fuse length, link width at the end, plate thickness of the fuse, and fuse yield strength, respectively.

The structural members are designed using the load and resistance factor design (LRFD). Modified static analysis method and proposed three loading cases by Eatherton and Hajjar [25] are used to estimate amplified demands of controlled rocking archetypes. Figure 6 shows three load cases including an inverted triangular (Fig. 6(a)), upward triangular (Fig. 6(b)), and a reverse triangular (Fig. 6(c)) profiles. Tables 2 and 3 show the design properties and frame sections of the archetypes. Further details of archetypes designed are discussed in Ref. [31].

3.1 Nonlinear analysis model

To perform the nonlinear dynamic analysis of designed archetypes, the computational model is analyzed using Opensees software [42]. Figure 7 shows the detailed scheme of a two-dimensional model of the system. The boundary conditions of archetypes are modeled using gap elements with zero-length and elastic-no-tension material, which support compression only. Two leaning columns with no lateral stiffness are modeled on each side of the frame using "elastic beam-column," low-stiffness "rotational spring," and "rigid truss" elements to simulate the geometric nonlinearity with (P-Δ) effects. Note that gravity loads are applied at the rocking frame and leaning columns based on their tributary area and seismic mass is lumped at the frame nodes as shown in Fig. 7. Displacement-based nonlinear beam–column elements with four integration points and fiber cross-sections with nonlinear "Steel02"

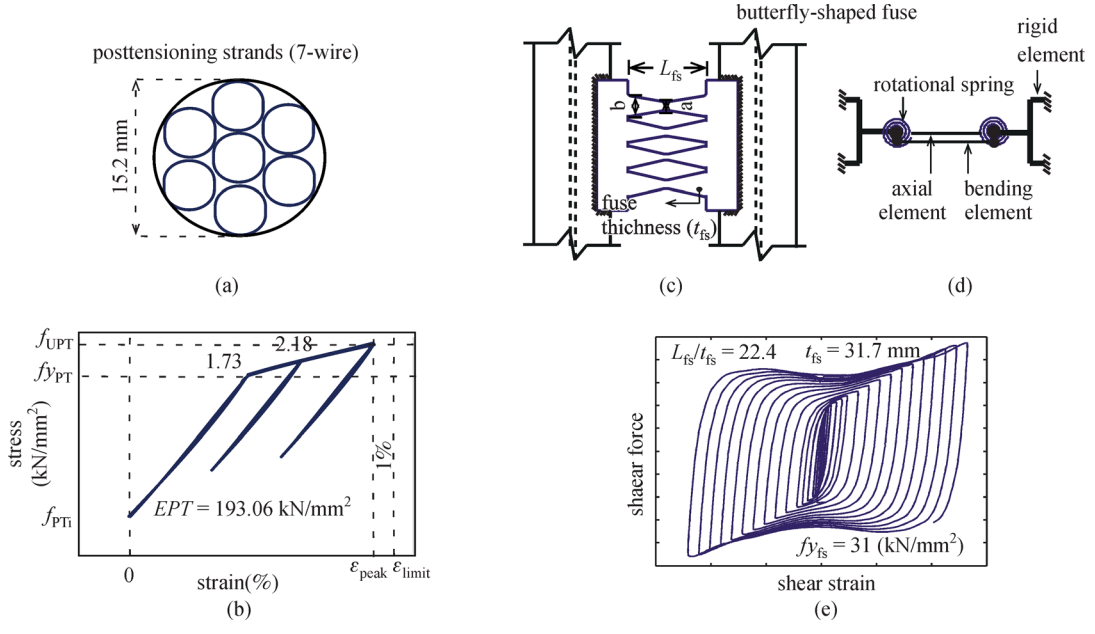

Fig. 5 (a) Configuration and (b) material of post-tensioning strand. (c) Configuration, (d) modeling, (e) and hysteretic behavior of butterfly-shaped fuse [41]

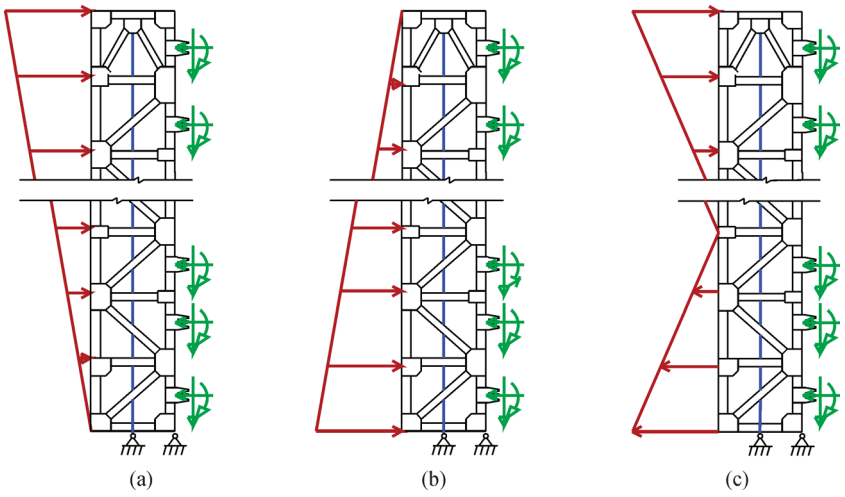

Fig. 6 Three design load cases. (a) Inverted triangular; (b) upward triangular; (c) reverse triangular profiles [13]

Table 2 Design properties of self-centering braced frame archetypes

	PG_1			PG_2			PG_3			PG_4		
	D_{max}/perimeter			D_{min}/perimeter			D_{max}/space			D_{min}/space		
	3-st.	6-st.	9-st.	3-st.	6-st.	9-st.	3-st.	6-st.	9-st.	3-st.	6-st.	9-st.
	A_1	A_2	A_3	A_4	A_5	A_6	A_7	A_8	A_9	A_{10}	A_{11}	A_{12}
F_{Pti} (kN)	2062	3689	7256	768	743	1345	1543	2652	3305	249	300	425
A_{PT} (cm^2)	22	28	52	8.3	5.7	9.7	16.8	20	41	2.7	2.6	3.1
N_{PT}	16	20	30	6	4	7	12	15	30	2	2	2
V_{fP}(kN)	280	256	318	139	96	105	280	256	318	139	96	105
N_{fs}–N_{lfs}	3–8	6–8	9–10	3–4	3–4	3–6	3–8	6–8	9–10	3–4	3–4	3–6

material are used to model the beam, column, and brace elements (Fig. 7). Beam-column connection is shear tab type that is modeled using concentrated rotational spring elements [43].

The braces are divided into ten nonlinear fiber elements for accurate modeling of in-plane (global) and local brace-buckling behaviors (Fig. 8(a)). For this purpose, each brace is modeled with initial geometric imperfection equal to 0.001 of its effective length (L_{eff} /1000) using subdivided nonlinear beam-column elements. In addition, the wide fiange braces are discretized by 2 fibers in thickness and 10 fibers along the flange and web of the braces, respectively (Fig. 8(a)). The braces are connected to the column and beam elements through gusset plate connections. The gusset plate connections (Fig. 8(b)) are modeled using a combination of force-based beam-column elements with 2 integration points and elastic beam-column elements.

The PT strands are modeled using a corotational truss element that is connected at the bottom to the stiff springs act in tension only (Fig. 7). The tri-linear push curve (Fig. 7(a)) constructed using a series combination of elastic-perfectly plastic and hysteretic materials to capture both initial post-tensioning stress, f_{PTi}, and strength degradation of PT strands. As shown in Fig. 7(b), the first linear branch of this material behavior is increased from f_{PTi} with modulus of elasticity of E_{PT} and terminated at the yield strength (f_{yPT}). When f_{yPT} is attained, the PT material initiates to yield and follows a hardening branch ($\alpha_{h,PT}E_{PT}$) to the ultimate tensile strength (f_{uPT}); f_{uPT} is the beginning of post-peak point in the degrading branch ($\alpha_{pc,PT}E_{PT}$). The initial strain (ε_i), yield strain (ε_y), ultimate strain (ε_u), and fracture strain (ε_m) correspond to the strength of f_{PTi}, f_{PTy}, f_{uPT}, and zero, respectively. The values of ε_u and ε_m are assumed to be 1 and 5%, respectively [14].

Two types of butterfly-shaped fuses, including non-degrading and degrading types, are recently developed and tested for self-centering braced frames [14]. The degrading fuses are made of thinner steel plates than the non-degrading ones, which allow buckling at lower shear deformations. In this study, thick steel shear plate fuses, with the slenderness ratio of 22.4, are used, which exhibit a stable hysteresis loops in flexure and undergo torsional-flexural buckling at a large shear strain. Figure 6(c) shows the detailed model of the butterfly-shaped fuses, which is modeled explicitly with a displacement-based

Table 3 Brace, beam, and column sections of self-centering archetypes

story no.	seismic design category (SDC)							
	brace section		beam section		middle column section		side column section	
	D_{max}	D_{min}	D_{max}	D_{min}	D_{max}	D_{min}	D_{max}	D_{min}
1	W14×74	W14×61	W14×34	W14×30	W14×233	W14×176	W14×90	W14×74
2	W14×82	W14×68	W14×30	W14×30	W14×233	W14×176	W14×90	W14×74
3	W14×90	W14×74	W14×38	W14×34	W14×233	W14×176	W14×90	W14×74
1	W14×68	W14×53	W14×30	W14×30	W14×311	W14×257	W14×159	W14×132
2	W14×68	W14×53	W14×30	W14×30	W14×311	W14×257	W14×159	W14×132
3	W14×68	W14×53	W14×30	W14×30	W14×311	W14×257	W14×159	W14×132
4	W14×68	W14×53	W14×30	W14×30	W14×211	W14×176	W14×120	W14×99
5	W14×68	W14×53	W14×34	W14×30	W14×211	W14×176	W14×120	W14×99
6	W14×90	W14×74	W14×34	W14×30	W14×211	W14×176	W14×120	W14×99
1	W14×90	W14×74	W14×30	W14×30	W14×500	W14×370	W14×311	W14×257
2	W14×90	W14×74	W14×34	W14×30	W14×500	W14×370	W14×311	W14×257
3	W14×90	W14×74	W14×34	W14×30	W14×500	W14×370	W14×311	W14×257
4	W14×90	W14×74	W14×34	W14×30	W14×398	W14×370	W14×257	W14×233
5	W14×90	W14×74	W14×34	W14×30	W14×398	W14×370	W14×257	W14×233
6	W14×90	W14×74	W14×34	W14×30	W14×398	W14×370	W14×257	W14×233
7	W14×90	W14×74	W14×34	W14×30	W14×311	W14×257	W14×145	W14×120
8	W14×99	W14×82	W14×34	W14×30	W14×311	W14×257	W14×145	W14×120
9	W14×145	W14×99	W14×34	W14×30	W14×311	W14×257	W14×145	W14×120

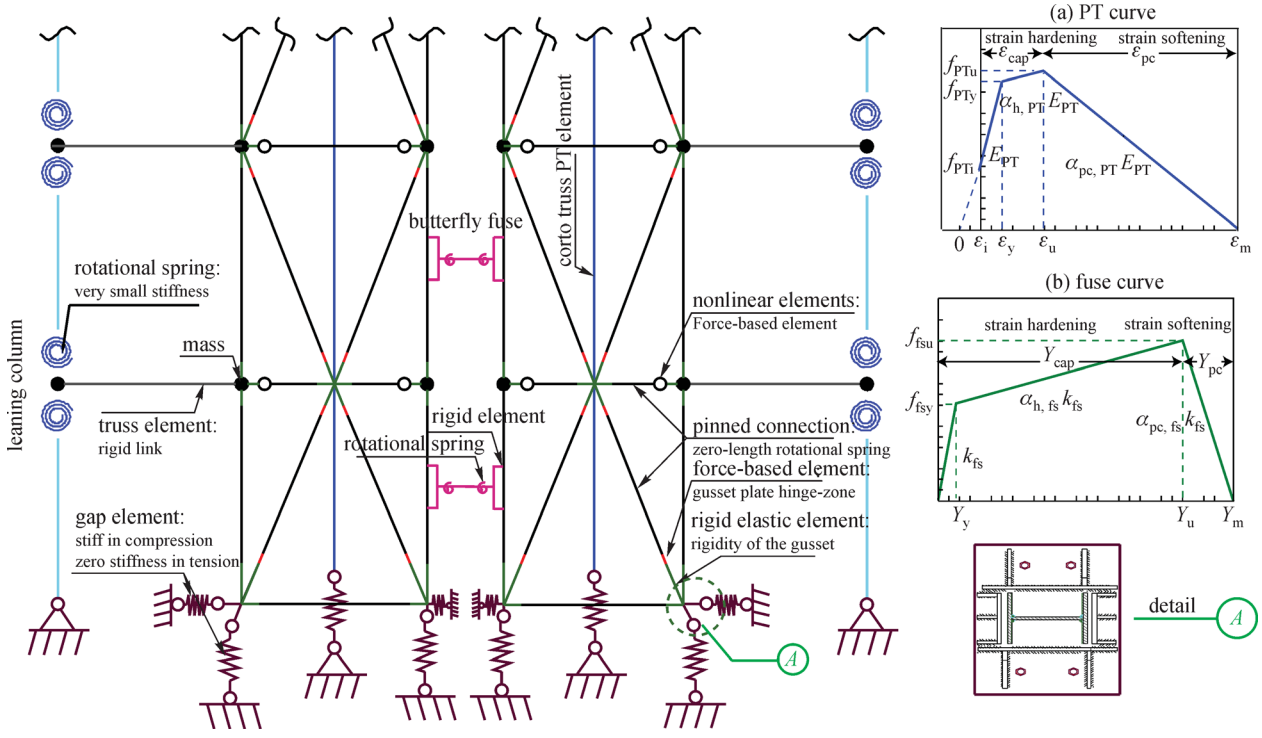

Fig. 7 Nonlinear simulation of self-centering archetypes in OpenSees

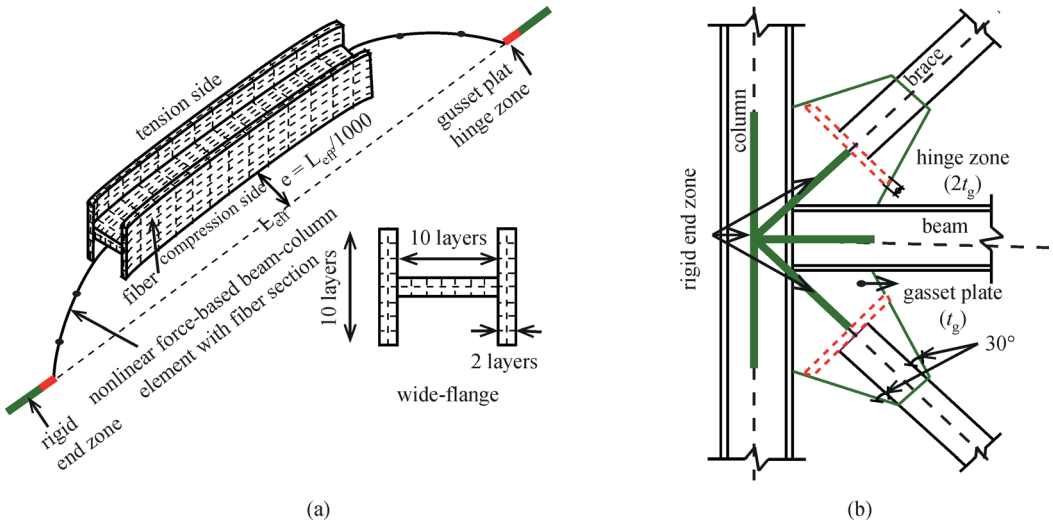

Fig. 8 (a) Brace with gusset-plate model; (b) details of gusset plate connection

beam-column elements using fiber sections, and rotational springs are used to simulate the axial, flexural, and lateral-torsional buckling behaviors of fuses (Fig. 7(b)) [13]. Rigid parts at the ends of the fuse are modeled with elastic beam-column element constrained to the frames using the equal DOF command. A hysteretic material is used to simulate the degrading and fracture behavior of fuses through zero-length rotational springs as the link buckles. The fiber displacement-based elements with the steel-01 material are used along the length of fuses to capture their hysteretic flexural and tensile behavior. The thickness and average depth of the fuse links are set as the properties of fiber section. Figure 7(b) shows the ideal tri-linear backbone behavior. Using this modeling, the fuse links can initiate to yield while their shear strength reaches yield strength (f_{fsy}) and then increases to fracturing strength (f_{ufs}) through a hardening branch ($\alpha_{h,fs}k_{fs}$). According to the previous experimental tests on the fuse subassembly, fracturing of the fuse is assumed to occur at 35% shear strain (γ_m) followed by a steep drop in strength (Fig. 7(b)) [13]. As shown in Fig. 7(b), the shear strength drops to zero with steep stiffness ($\alpha_{pc,fs}k_{fs}$) after initiating the fracture at the large shear deformation. Note that the fracturing point corresponding 35% shear strain (γ_m) and fuse shear strength (V_{fp}) is considered as the fuse fracture limit.

4 Hazard curves and ground motions set

To perform incremental dynamic analysis (IDA) and safety assessment, site hazard curves and 44 far-field ground motions (22 pairs) adapted from FEMA P695 [44]. As mentioned earlier, the archetypes are assumed to be located in Los Angeles, California, and soil class D is used. Figure 9(a) shows the mean hazard curves, $\lambda_{Sa}(Sa(T_1))$, for the A_1, A_2, and A_3 archetypes with conditioning periods (first mode periods) of T_{A1} = 0.8s, T_{A2} = 1s, and T_{A3} = 2s and 5% of damping. The seismic hazard curves are taken from the United States Geological Survey (USGS) website for a given site. Each ground motion hazard curve provides the MAF of exceedance of a particular spectral acceleration for a given period and damping ratio [34]. To use a site hazard curves in closed-form safety integral, two rates of exceedance ($-\ln(1-risk\%)/years$), equal to 0.00211 and 0.0044 (i.e., 10%-in-50 and 2%-in-50 years probability of exceedance), are considered for each of the individual archetypes, as shown in Fig. 9(a). Figure 9(b) shows the spectral acceleration of the unscaled far-field record set and the characteristics of these ground motions are listed in Table A1, of appendix A. The ground motion set, composed of 22 component pairs of horizontal ground motions, taken from 14 events.

5 Performance evaluation

5.1 Nonlinear analysis results

For twelve self-centering archetypes, the incremental dynamic analysis is carried out for the given ground motion set. Figure 10(a) shows the maximum inter-story drift ratio (IDR_{max}) responses for A1, A2, and A3 archetypes in terms of spectral acceleration intensity (Sa). Each point of these IDA curves is derived from nonlinear time history analysis (NTHA). For example, the NTHA results of A3 archetype under the scaled Hector Mine ground motion, 1999 to PGA of 0.27 and 1.91 g are shown in Fig. 10. As shown in Figs. 10(b), for the scaled case to PGA of 1.91 g, the strands are yielded at about 6s and 3% RDR and its maximum roof drift ratio (RDR_{max})

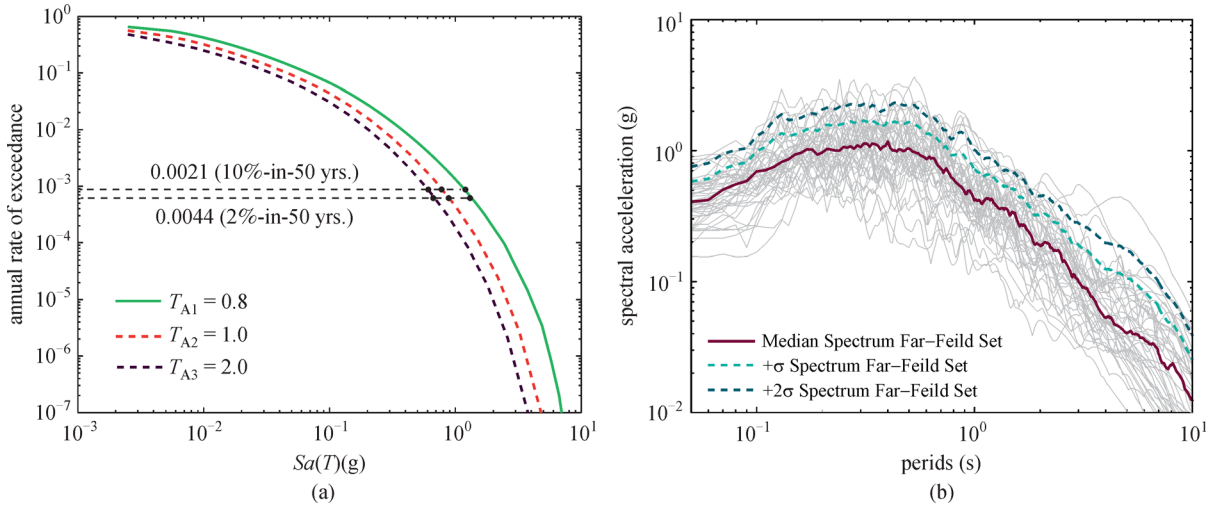

Fig. 9 (a) Ground motion hazard curves for the archetypes of PG_1 (A_1, A_2, and A_3); (b) spectral accelerations and median spectrum of far-field FEMA P695 ground motion set.

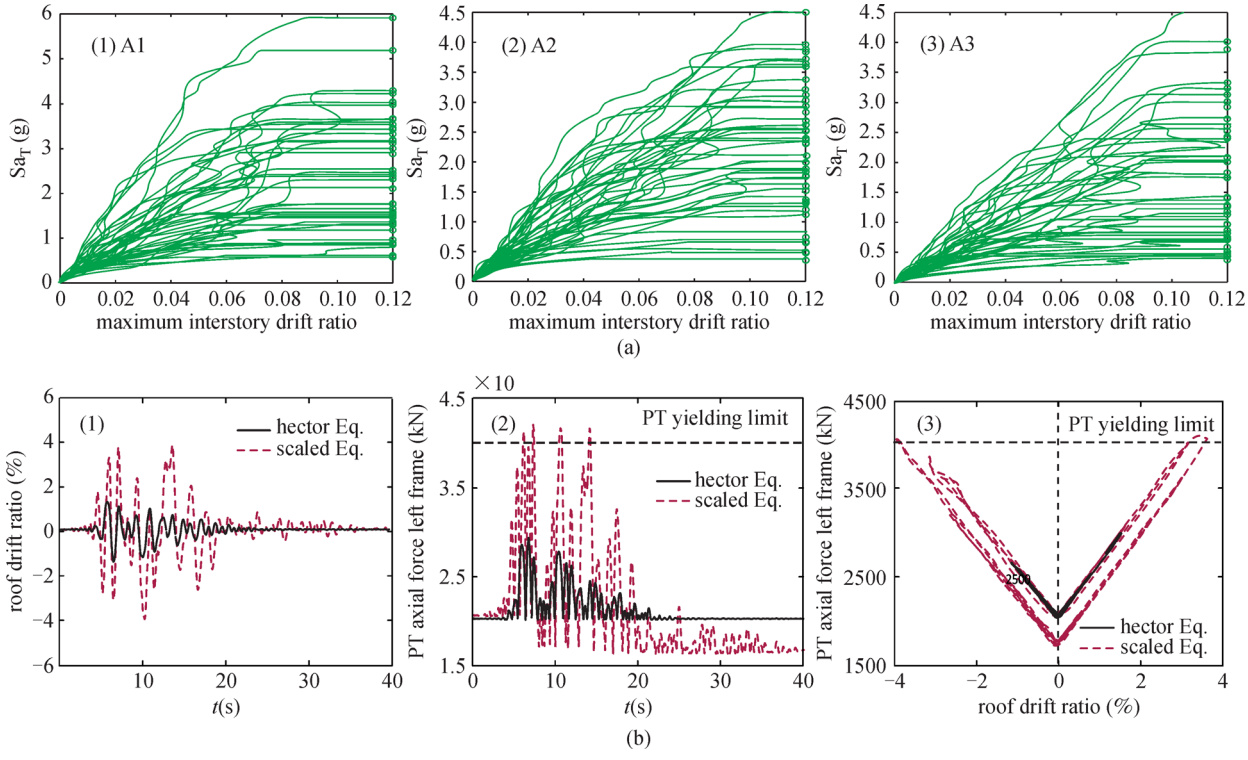

Fig. 10 (a) IDAs of (1) A_1, (2) A_2, and (3) A_3 archetypes under a set of selected ground motions; (b) (1) roof drift ratio, (2) PT axial force versus time and (3) roof drift ratio for the A3 archetype under the scaled horizontal component of Hector Mine earthquake to PGA of 0.27 and 1.91 g

and PT axial force (Fig. 10(b)) are 3 and 1.43 times of other case, respectively.

5.2 Performance levels and limit-states

To perform a probabilistic safety assessment, it is required to obtain fragility curves of archetypes at desired performance levels. In this paper, three performance levels including Immediate Occupancy (IO), life safety (LS), and Collapse Prevention (CP) are defined for self-centering archetypes. The large nonlinearity of structural elements and global instability of structure are considered as the IO and CP limits, and LS level is assumed as the intermediate level between IO and CP levels. Figure 11 shows the ideal

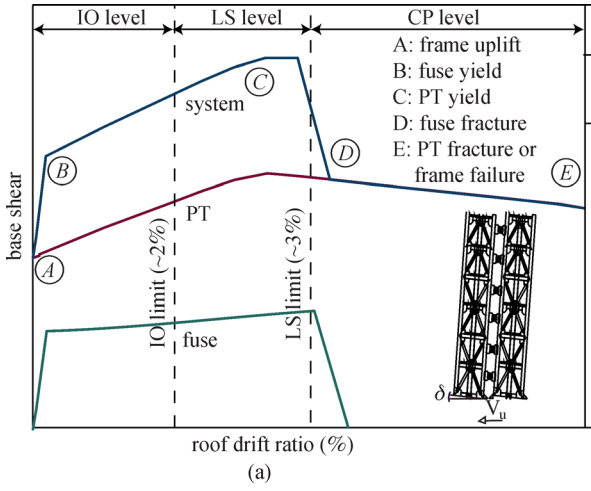

limit-state	performance objective (hazard intensity/inter-story drift ratio) UO (DBE/0.02)	LS (DBE-MCE/0.03)	CP (>MCE/0.09)
(A) frame uplift	yes	yes	yes
(B) fuse yield	yes	yes	yes
(C) PT yield	no	yes	yes
(D) fuse fracture	no	no	yes
(E) PT fracture or	no	no	no
(E) frame failure	no	no	no

(b)

Fig. 11 (a) Idealized schematic lateral force-drift ratio of self-centering systems; (b) definition of performance levels and limit-states

pushover curve, definition, and relations between defined limit states and performance levels at DBE and MCE intensity levels. In general, it is assumed that five limit states including frame uplift (points *A*), fuse yield (point *B*), PT yield (point *C*), fuse fracture (point *D*), PT fracture, and severe nonlinearity of structural elements (point *E*) can occur in ideal self-centering systems from low to high seismic intensities. In addition, pushover curve consists of two branches at IO level. In the first branch (*A*-*B*), the frame uplift, fuses yield, and the system behaves elastically and, then, reaches to fuse yield point and continues with a post-yield hardening branch (*B*-*C*). At LS level, the curve is followed by PT yield limit (point *C*), which is terminated at ultimate strength of PT strands (capping point). At the CP level, fuses are first fractured (point *D*) in the post-capping phase (branch 3) and, then, strength and stiffness of the system are initiated to degrade due to the loss of PT strength, buckling braces, and members or connection fracture (branch 4). Therefore, considering this hierarchical behavior, it is expected that the frame members and PT strands to be remain elastic under design-basis ground motions (10%-in-50 years) and prevent severe strength and stiffness degradation under MCE ground motions (2%-in-50 years).

Three main limit states including initiating PT yield, fuse fracture, and global collapse of self-centering archetypes are quantified in this paper. The spectral acceleration intensities and inter-story drifts of three limit states for representative samples (A1, A2, and A3) under each ground motion are plotted in Fig. 12. To quantify IDRs of PT yield (LS(1); red points) and fuse fracture (LS(2); green points) limit states at each Sa intensity level, the PT axial force and fuse shear force for each archetype are compared with PT yield strength and fuse fracture capacity, respectively. The main collapse modes of self-centering systems could be buckling of the braced frame, the collapse of the gravity frame, or overturning of the frame due to PT strands or fuse fracture. In this study, collapse modes related to the failure of the fuse, PT strands, and the members are considered in the numerical model to capture collapse capacity points. The collapse possibility of the gravity system is neglected. As shown in Fig. 12, the global collapse points of the archetypes (i.e., collapse spectral intensities and corresponding collapse IDRs) are quantified from IDA curve. The onset of the archetype collapse under a ground motion record is identified as the point where IDA curve become flat at a spectral intensity level that causes collapse. In other words, the collapse limit state is defined as the *Sa* intensity at which very small increase in the Sa level is caused a significant increase in the IDRs. From IDA results, it is observed that the PT fracture along with the strength and stiffness degradation of the braced frame members are the main causes of global collapse. Median values of limit state points for all archetypes are listed in Table 4. Results indicate that the mean spectral acceleration intensity ($\hat{S}_{LS}$) of PT yield, fuse fracture, and collapse capacity limit states range from 0.67 g to 1.04 g, 0.73 g to 1.25 g, and 0.85 g to 1.75 g, respectively, and their mean IDRs range from 0.32 to 0.38, 0.43 to 0.45, and 0.53 to 0.88, respectively. Another result is that the modeling parameters and seismic design category of archetypes affect the mean spectral capacity, $\hat{S}_{LS}$. For example, an increase of archetypes height led to a decrease of spectral intensities, and perimeter archetypes at SDC $D_{\max}$ could sustain larger spectral intensities than the space archetypes at SDC $D_{\min}$.

The 2%, 3%, and 8% inter-story drift ratios are defined qualitatively as IO, LS, and CP limit levels (Fig. 11(a)). To examine the efficiency of these definitions, the derived IDR values from IDAs of archetypes are compared with defined limit-state values (Fig. 11). As shown in Fig. 12, the defined performance objectives have occurred in the range of expected levels. For example, fuses fracture have occurred beyond 3% inter-story drift ratio (LS limit). As a

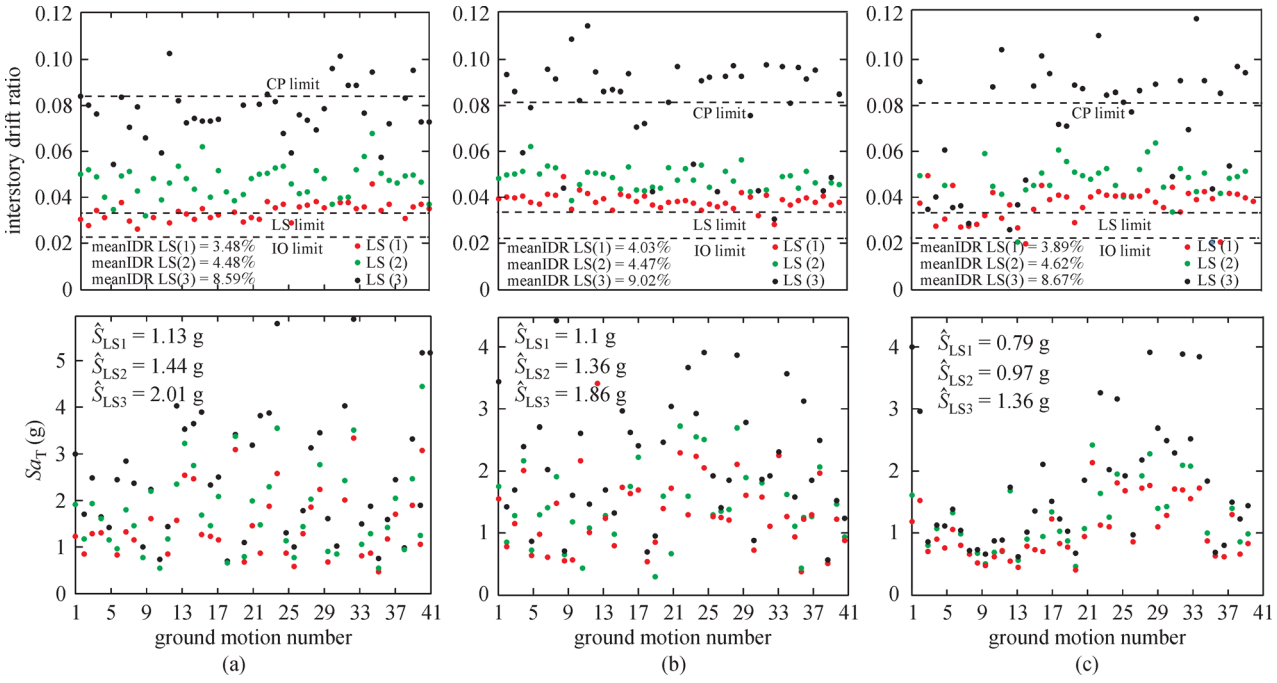

Fig. 12 Quantified PT yield (LS(1); red plus), fuse fracture (LS(2); green plus), and global collapse (LS(3); black plus) limit-state points (IDR and Sa) for (a) A_1, (b) A_2, and (c) A_3 archetypes

Table 4 Summary of the pushover and IDA results for self-centering archetypes

archetype ID	design configuration			$\hat{S}_{LS}$ (g)			mean IDR_{LS} (%)		
	number of stories	gravity loads	seismic design category	LS(1) [a]	LS(2) [b]	LS(3) [c]	LS(1) [a]	LS(2) [b]	LS(3) [c]
performance group number PG_1: SDC D_{max} and low gravity loading (perimeter frame)									
A_1	3	low	D_{max}	1.13	1.44	2.01	3.48	4.48	8.59
A_2	6	low	D_{max}	1.10	1.35	1.86	4.03	4.47	9.02
A_3	9	low	D_{max}	0.89	0.97	1.37	3.89	4.62	8.67
mean of performance group				1.04	1.25	1.75	3.80	4.52	8.76
performance group number PG_2: SDC D_{min} and low gravity loading (perimeter frame)									
A_4	3	low	D_{min}	0.75	0.86	1.14	3.40	4.33	5.56
A_5	6	low	D_{min}	0.71	0.82	0.96	3.62	4.81	5.49
A_6	9	low	D_{min}	0.61	0.64	0.70	3.17	4.15	5.23
mean of performance group				0.69	0.77	0.93	3.34	4.43	5.43
performance group number PG_3: SDC D_{max} and high gravity loading (space frame)									
A_7	3	high	D_{max}	0.91	1.02	1.33	3.44	4.41	7.35
A_8	6	high	D_{max}	0.88	0.97	1.27	3.87	4.73	7.80
A_9	9	high	D_{max}	0.78	0.86	0.97	3.76	4.56	7.52
mean of performance group				0.86	0.95	1.19	3.69	4.57	7.56
performance group number PG_4: SDC D_{min} and high gravity loading (space frame)									
A_{10}	3	high	D_{min}	0.73	0.81	1.05	3.29	4.13	5.22
A_{11}	6	high	D_{min}	0.69	0.76	0.81	3.12	4.42	5.17
A_{12}	9	high	D_{min}	0.61	0.63	0.69	3.22	4.21	5.41
mean of performance group				0.67	0.73	0.85	3.21	4.25	5.29

[a] LS(1): PT yield; [b] LS(2): fuse fracture; [c] LS(3): global collapse

result, 2, 3, and 8% inter-story drift ratios can be considered for this type of self-centering systems as IO, LS, CP limit levels.

5.3 Aleatory and epistemic uncertainties

According to the procedure of PSA analysis, it is required to quantify sources of aleatory (randomness) and epistemic uncertainties. The total aleatory uncertainty ($\beta_{\text{total},R}$) arises from the inherent randomness of demand and capacity of a structure due to the nature of earthquakes, which can be determined as follows [33]:

$$\beta_{\text{total},R} = \sqrt{\beta_{EDP,R}^2 + \beta_{C,R}^2}, \tag{12}$$

where $\beta_{EDP,R}$ and $\beta_{C,R}$ denote record-to-record (RTR) variability of demand and capacity parameters of a structure, respectively.

This paper quantifies the aleatory randomness, $\beta_{EDP,R}$ of archetypes by the following equation using fractiles IDA curves [27]:

$$\beta_{EDP,R|16} = \beta_{16} = \log\left(\frac{f_{50}}{f_{16}}\right),$$

$$\beta_{EDP,R|84} = \beta_{84} = \log\left(\frac{f_{84}}{f_{50}}\right), \tag{13}$$

where f_{16}, f_{50}, and f_{84} are the 16th, 50th (median), and 84th fractile IDAs and $\beta_{EDP,R|16}$ and $\beta_{\text{EDP,R|84}}$ indexes are their RTR variability.

Figure 13(a) shows fractiles of archetypes determined by cross-sectional method [45]. Also, both $\beta_{EDP,R|16}$ and $\beta_{EDP,R|84}$ measures are plotted in terms of $IDR_{\max}$ versus $Sa[\beta_{\text{DR}}(IDR_{\max}|Sa)]$ (Fig. 13(b)) and Sa versus $IDR_{\max}$ $[\beta_{EDP,R}(Sa|IDR_{\max})]$ (Fig. 13(c)). As shown, RTR variability of $\beta_{EDP,R}$ of archetypes is generally increased by increasing Sa (Fig. 13(b) intensity level or $IDR_{\max}$ (Fig. 13 (c)) demand. The maximum value of $\beta_{EDP,R}$ of archetypes is almost equal to 0.35 (Fig. 13(b)). Note that, according to previous studies [46,47], the collapse uncertainty of conventional buildings range from 0.30 to 0.45 [48]. The aleatory variability of capacity values ($\beta_{C,R}$) can be determined from the experimental or analytical data. Based on the dispersion of collapse capacity points obtained from IDA results, $\beta_{C,R}$ of self-centering archetypes is equal to 0.4. Therefore, using Eq. (12), the total RTR variability, $\beta_{\text{total},R}$, is equal to 0.5.

The epistemic uncertainty (β_{TU}), as another type of uncertainty, arises from the ignorance or lack of knowledge, can be obtained by the following equation [49]:

$$\beta_{\text{total},U} = \sqrt{\beta_{Des}^2 + \beta_{TD}^2 + \beta_{MDL}^2}, \tag{14}$$

where β_{Des}, β_{TD}, and β_{MDL} are uncertainties related to design requirements, test data, and modeling, respectively.

There are several methods to quantify the components of epistemic uncertainty. Monte Carlo simulation and first-order second moment (FOSM) are the methods have been commonly used [49–52] for quantifying β_{MDL}. In this paper, total epistemic uncertainty, $\beta_{\text{total},U}$, of the archetypes is determined using the predefined values suggested by FEMA P695 [44]. According to FEMA P695, constant values of 0.1, 0.2, 0.35, and 0.5 are suggested for translating quality ratings of superior, good, fair, and poor assigned to design requirements, test data, and nonlinear models of archetypes, respectively.

The quality rankings of design requirements and numerical modeling are assumed to be good-quality (β_{DR} = 0.2), and test data for the self-centering archetypes are high-quality (β_{TD} = 0.1). Therefore, using Eq. (14), the total epistemic uncertainty is obtained equal to, $\beta_{\text{total},U}$ = 0.3.

Finally, the total uncertainty ($\beta_{TOT} = \sqrt{\beta_{TR}^2 + \beta_{TU}^2}$) of archetypes equal to square root of the sum of squares (SRSS) of epistemic and aleatory uncertainty is estimated β_{total} = 0.6.

Figure 14 shows the effects of total uncertainty, β_{TOT}, compared with RTR uncertainty, β_{TR}, on the fragility curves of the representative archetypes. As mentioned before, the fragility curve is a probabilistic tool that indicates the correlation between probability of exceeding a given limit state and seismic intensity [53]. Considering $\hat{S}_{LS}$ and β_{TR}, fragility curves of archetypes are first plotted using the lognormal fitting method on IDA points at each limit state and then adjusted by the total uncertainty, $\beta_{TOT.}$ As shown in Fig. 14, for spectral intensities of higher than $\hat{S}_{LS}$, the probability of exceeding $\hat{S}_{LS}$ of adjusted fragility curves is lower than the lognormal one.

5.4 Margin of safety, confidence level, and safety assessment

The margin of safety against the occurrence of a given limit state for archetypes can be determined as the ratio of median spectral acceleration, $\hat{S}_{LS}$, (i.e., 50% probability of exceedance) to MCE spectral intensity, S_{MT} (i.e., 2% probability of exceedance). The safety margin ratio for archetypes at defined limit states along with S_{MT} and $\hat{S}_{LS}$ values are shown in Fig. 14 and listed in Table 5. As shown, safety margin ratio for PT yield, fuse fracture, and global collapse limit states range from 1.52 to 4.17, 1.17 to 3.76, and 1.05 to 3.59, respectively. This result indicates that the archetypes provide a large margin of safety under MCE ground motions against the occurrence of undesirable limit-states. Moreover, the safety margin ratios are increased with increasing the height of the archetypes and for perimeter archetypes at SDC $D_{\max}/D_{\min}$ are higher than the space archetypes at SDC $D_{\max}/D_{\min}$.

Using SAC/FEMA confidence-based format, the confidence level, X, of self-centering archetypes in the

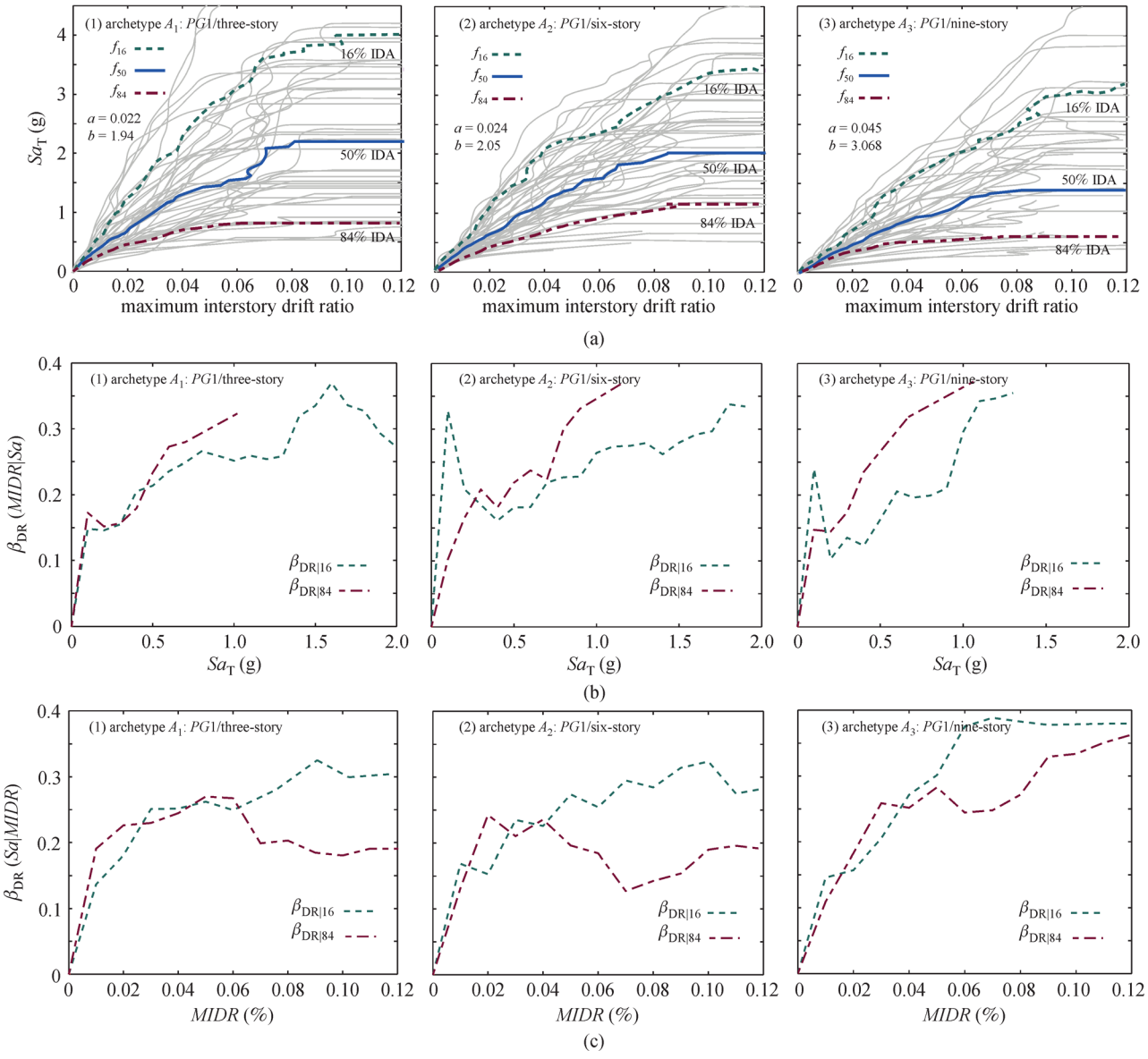

Fig. 13 (a) Fractile IDA curves and record-to-record uncertainty of (b) maximum inter-story drift (IDR_{max}) versus Sa ($\beta_{DR}(IDR_{max}|Sa)$) and (c) Sa versus IDR_{max} ($\beta_{DR}(Sa|IDR_{max})$) for (1) A_1, (2) A_2, and (3) A_3 archetypes

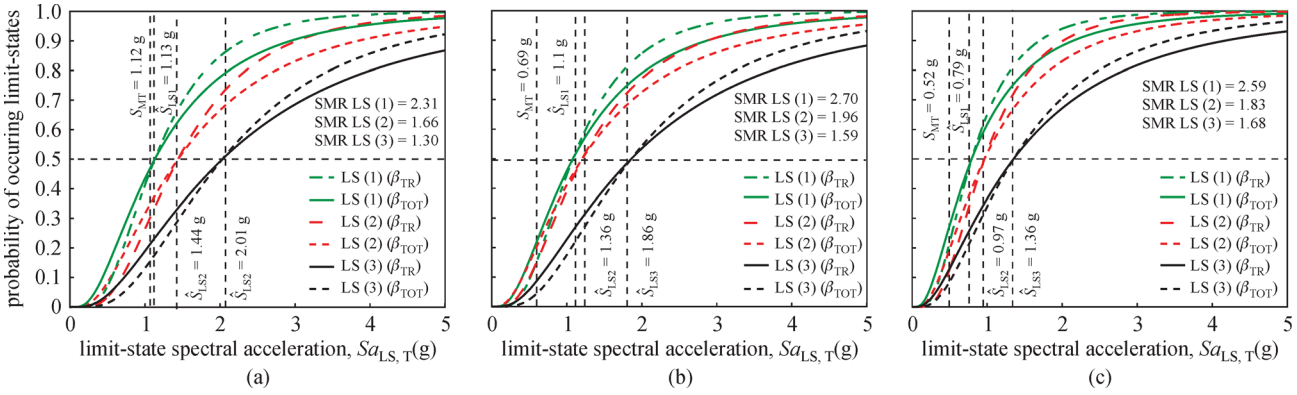

Fig. 14 Lognormal and adjusted fragility curves for PT yield, fuse fracture, and global collapse limit states of (a) A_1, (b) A_2, and (c) A_3 archetypes.

predefined limit states are determined using K_X (Eq. (6)) and λ_X (Eq. (7)) parameters, as summarized in Table 5. The confidence levels for the PT yield, fuse fracture, and global collapse limit states range from 93.98 to 99.98%, 83.87 to 99.74%, and 68.13 to 85.60%, respectively, and their mean values are 97.91%, 93.84%, and 78.93%, respectively. As can be seen, more than 90 and 80% confidence level is satisfied for PT yield and fuse fracture limit states at 10 and 2% probability of exceedance, but the confidence level for global collapse limit state is relatively low. However, more than 60% confidence level is contributed in satisfying collapse prevention. Hence, in conclusion the confidence associated with the three main limit states, the designed archetypes provide the large level of confldence at 10% in 50 yrs. and 2% in 50 yrs. return period.

For the probabilistic safety assessment and verifying the efficiency of the design procedure, the MAF of exceeding the inter-story drift ratio of the archetype at defined limit-states, λ_{IDR}^{LS}, is compared with the acceptable mean annual frequency, λ^{P_0}. Figure 15(a) shows the derivative of λ_{IDR}^{LS} spectra and λ_{IDR}^{LS} values for the sample archetypes at the predefined limit states, and λ_{IDR}^{LS} for all the archetypes are summarized in Table 6. As shown, the mean annual frequency for PT yield, fuse fracture, and global collapse limit states, range from 1.64×10^{-4} to 3.41×10^{-4}, 1.23×10^{-4} to 2.78×10^{-4}, and 0.67×10^{-4} to 1.96×10^{-4}, respectively, and their mean values are 2.30×10^{-4}, 2.07×10^{-4}, and 1.54×10^{-4}, respectively. This result indicates that λ_{IDR}^{LS} of PT yield limit is higher than that of fuse fracture and collapse limit-states. For example, MAFs of PT yield [$\lambda^{LS(1)}$], fuse fracture [$\lambda^{LS(2)}$], and global collapse [$\lambda^{LS(3)}$] for A_1 archetype are 0.004, 0.013, and 0.05, respectively, as shown in Fig. 15(a). As a result, the probability of PT yield is lower than another limit states due to its lower capacity. According to Eq. (2), to the safety assessment of the archetypes, the MAF of performance objectives (P_0), equal to $\lambda^{P_0} = -\ln(1-n\%)/yrs.$ are determined at the desired seismic intensity levels. The DBE (10% probability of exceedance in 50 years) and MCE (2% probability of exceedance in 50 years) hazard levels are chosen here as desired design intensity level. For these two rates of exceedance, λ^{P_0} are equal to $\lambda^{P_0} = -\ln(1-0.1)/50 = 0.00211$ and $\lambda^{P_0} = -\ln(1-0.02)/50 = 0.00044$, respectively. In each intensity level and limit-state, acceptance criteria of λ^{P_0} are compared to λ_{IDR}^{LS} of archetypes, as shown in Table 6. Results indicate that the archetypes are able to meet the desired performance objectives. Therefore, the procedure and assumptions for archetypes design provide the large margin of safety and satisfy the desired acceptance criteria. Moreover, as can be

Table 5 Summary of IDA results, safety margin ratios, and confidence levels of self-centering archetypes at defined limit states.

archetype ID	design configuration			$\hat{S}_{LS}$ (g)			safety margin ratio			confidence level of x (%)		
	number of stories	gravity/SDC loads	S_{MT} (g)	LS(1)[a] 10%/50	LS(2)[b] 2%/50	LS(3)[c] 2%/50	LS(1) [a]	LS(2) [b]	LS(3) [c]	LS(1) [a]	LS(2) [b]	LS(3) [c]
performance group number PG_1: SDC D_{max} and low gravity loading (perimeter frame)												
A_1	3	low/D_{max}	0.87	1.13	1.44	2.01	2.31	1.66	1.30	96.08	83.87	77.08
A_2	6	low/D_{max}	0.69	1.10	1.35	1.86	2.70	1.96	1.59	99.98	94.87	79.57
A_3	9	low/D_{max}	0.53	0.89	0.97	1.37	2.59	1.83	1.68	98.32	91.22	81.69
mean of performance group			0.69	1.04	1.25	1.75	2.54	1.82	1.51	98.12	89.98	79.44
performance group number PG_2: SDC D_{min} and low gravity loading (perimeter frame)												
A_4	3	low/D_{min}	0.37	0.75	0.86	1.14	3.08	2.32	2.03	99.98	91.61	85.69
A_5	6	low/D_{min}	0.23	0.71	0.82	0.96	4.17	3.57	3.09	99.18	99.01	79.00
A_6	9	low/D_{min}	0.17	0.61	0.64	0.70	4.12	3.76	3.59	98.22	99.74	85.60
mean of performance group			0.26	0.69	0.77	0.93	3.58	2.96	2.65	99.12	96.78	84.76
performance group number PG_3: SDC D_{max} and high gravity loading (space frame)												
A_7	3	high/D_{max}	0.87	0.91	1.02	1.33	1.52	1.17	1.05	93.98	85.53	78.88
A_8	6	high/D_{max}	0.69	0.88	0.97	1.27	1.80	1.40	1.27	96.12	97.19	70.00
A_9	9	high/D_{max}	0.53	0.78	0.86	0.97	1.83	1.62	1.47	97.37	93.63	74.85
mean of performance group			0.69	0.86	0.95	1.19	1.70	1.35	1.22	95.82	92.11	74.57
performance group number PG_4: SDC D_{min} and high gravity loading (space frame)												
A_{10}	3	high/D_{min}	0.37	0.73	0.81	1.05	2.84	2.19	1.97	97.35	92.15	83.33
A_{11}	6	high/D_{min}	0.23	0.69	0.76	0.81	3.52	3.30	3.00	99.38	98.02	79.42
A_{12}	9	high/D_{min}	0.17	0.61	0.63	0.69	4.06	3.71	3.59	99.05	99.31	68.13
mean of performance group			0.26	0.67	0.73	0.85	3.27	2.81	2.58	98.59	96.49	76.96

[a] LS(1): PT yield; [b] LS(2): fuse fracture; [c] LS(3): global collapse

Table 6 Performance evaluation of self-centering archetypes

archetype ID	design configuration			$\lambda^{LS}_{(\times 10^{-4})}$			$\lambda^{P_0}_{(\times 10^{-4})}$		acceptance check		
	number of stories	gravity loads	SDC	LS(1)[a] 10%/50	LS(2)[b] 2%/50	LS(3)[c] 2%/50	10%/50	2%/50	LS(1)[a]	LS(2)[b]	LS(3)[c]
performance group number PG_1: SDC D_{max} and low gravity loading (perimeter frame)											
A_1	3	low	D_{max}	3.02	1.90	1.11	21	4	pass	pass	pass
A_2	6	low	D_{max}	1.64	1.71	0.67	21	4	pass	pass	pass
A_3	9	low	D_{max}	1.90	1.23	0.80	21	4	pass	pass	pass
mean of performance group				2.19	1.61	0.86	21	4	pass	pass	pass
performance group number PG_2: SDC D_{min} and low gravity loading (perimeter frame)											
A_4	3	low	D_{min}	3.41	2.34	1.45	21	4	pass	pass	pass
A_5	6	low	D_{min}	2.82	2.01	1.28	21	4	pass	pass	pass
A_6	9	low	D_{min}	3.08	2.78	1.83	21	4	pass	pass	pass
mean of performance group				3.10	2.38	1.52	21	4	Pass	Pass	pass
performance group number PG_2: SDC D_{min} and low gravity loading (perimeter frame)											
A_7	3	high	D_{max}	3.27	2.76	1.96	21	4	pass	pass	pass
A_8	6	high	D_{max}	2.21	1.83	1.12	21	4	pass	pass	pass
A_9	9	high	D_{max}	2.60	2.35	1.50	21	4	pass	pass	pass
mean of performance group				2.69	2.31	1.53	21	4	pass	pass	pass
performance group number PG_4: SDC D_{min} and high gravity loading (space frame)											
A_{10}	3	high	D_{min}	2.88	2.25	1.30	21	4	pass	pass	pass
A_{11}	6	high	D_{min}	1.84	1.77	0.97	21	4	pass	pass	pass
A_{12}	9	high	D_{min}	2.11	1.96	1.38	21	4	pass	pass	pass
mean of performance group				1.22	1.99	2.28	21	4	Pass	pass	pass

a) LS(1): PT yield; b) LS(2): fuse fracture; c) LS(3): global collapse

seen, the contributions of spectral intensity of about Sa = 0.4 g is more than other intensities toλ^{LS}_{IDR}.

6 Summary and conclusions

Self-centering special concentrically braced frame is known as low-damage system that can concentrate damage on replaceable fuses. This paper quantified main limit states of PT yield, fuse fracture, and global collapse limit states for self-centering archetypes. In addition, the safety performance of 12 low- and mid-rise self-centering braced frames with different frame types (space/perimeter) and seismic design categories (SDC D_{max}/SDC D_{min}) were determined using safety margin ratio, confidence level and mean annual frequency measures. The investigation resulted in the following main conclusions:

1) The mean values of spectral capacity intensities ($\hat{S}_{LS}$) for the PT yield, fuse fracture, and global collapse limit states ranged from 0.67 g to 1.04 g, 0.73 g to 1.25 g, and 0.85 g to 1.75 g, respectively, and mean of the corresponding maximum inter-story drift ratios (IDR_{max}) ranged from 0.32 to 0.38, 0.43 to 0.45, and 0.53 to 0.88, respectively. Moreover, based on defined performance levels for self-centering braced frames, IDR_{max} equal to 2%, 3%, and 8% were determined for performance limits of immediate occupancy, life safety, and global collapse, respectively. Furthermore, it was indicated that the mean spectral capacities of archetypes depends on modeling parameters and SDC.

2) It was shown that safety margin ratios for PT yield, fuse fracture, and global collapse limit states ranged from 1.52 to 4.17, 1.17 to 3.76, and 1.05 to 3.59, respectively, which showed that the self-centering braced frame provided a large margin of safety. In addition, it was found that mean values of confidence levels for these limit states were 97.91%, 93.84%, and 78.93%, respectively, in which more than 90 and 80% confidence level was satisfied for PT yield and fuse fracture limit states of self-centering braced frames at the 10% and 2% probability of exceedance; also, more than 60% was satisfied for collapse limit state. Furthermore, it was shown that safety margin ratios of the archetypes were increased with increasing the height of archetypes and perimeter self-centering archetypes at SDC D_{max}/D_{min} had larger safety margin ratio than space archetypes at SDC D_{max}/D_{min}. Also, confidence levels of avoiding limit states were decreased at high SDC (SDC D_{max}) relative to those located at low SDC (SDC D_{min}). As an important result, the designed archetypes were able to provide large margin ratio and level of

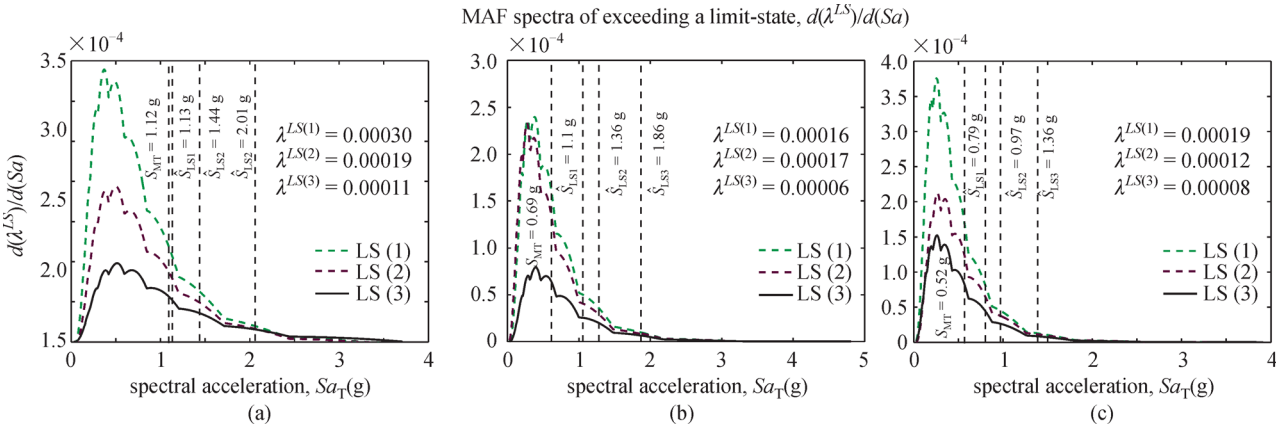

Fig. 15 Derivative MAF spectra of PT yield, fuse fracture, and global collapse limit states respecting $Sa(\mathrm{d}(\lambda_{\mathrm{LS}})/\mathrm{d}(Sa))$ for (a) A_1, (b) A_2, and (c) A_3 archetypes

confidence against the considered limit-states.

3) Mean values of MAF of limit-states, λ^{LS}, for PT yield, fuse fracture, and global collapse limit states were 2.30×10^{-4}, 2.07×10^{-4}, and 1.54×10^{-4}, respectively. It was shown that values of λ^{LS} for PT yield limit state were higher than those for fuse fracture and global collapse limit-states. Therefore, the probability of yielding PT strands was less than other considered limit-states. Moreover, by considering normalized spectral of derivative MAF, it was found that *Sa* intensity of 0.4 g had larger contribution on total MAF of exceedance than other seismic intensities.

4) Using safety assessment analysis, the validity of design procedure for the design of self-centering braced frame was verified by comparing MAF of limit states λ^{LS} with the desired acceptance criteria (MAF of P_0, λ^{P_0}). Results indicated that the designed archetypes with considered assumptions satisfied the acceptance criteria and met the desired performance objectives.

Appendix A

List of the far-field ground motion records prepared by FEMA P695 [44] (Table A1).

Table A1 Far-field ground motion record set [44]

ID	event	year	station	fault type	M_w [a]	T_g (s) Comp.1-2	distance (km)		$Vs30(m/s^2)$
							Clst.[b]	Epi.[c]	
1	Northridge	1994	Beverly Hills Mulhol	blind thrust	6.7	0.91-0.55	17.2	13.3	356
2	Northridge	1994	Canyon W Lost Cany	blind thrust	6.7	0.59-0.71	12.4	26.5	309
3	Duzce, Turkey	1999	Bolu	strike-slip	7.1	0.56-0.99	12.0	41.3	326
4	Hector Mine	1999	Hector	strike-slip	7.1	1.23-0.52	11.7	26.5	685
5	Imperial Valley	1979	Delta	strike-slip	6.5	3.28-1.66	22.0	33.7	275
6	Imperial Valley	1979	El Centro Array#11	strike-slip	6.5	1.76-0.74	12.5	29.4	196
7	Kobe, Japan	1995	Nishi-Akashi	strike-slip	6.9	0.47-0.72	7.1	8.7	609
8	Kobe, Japan	1995	Shin-Osaka	strike-slip	6.9	0.67-1.23	19.2	46	256
9	Kocaeli, Turkey	1999	Duzce	strike-slip	7.5	3.86-0.51	15.4	98.2	276
10	Kocaeli, Turkey	1999	Arcelik	strike-slip	7.5	1.24-9.28	13.5	53.7	523
11	Landers	1992	Yermo Fire Station	strike-slip	7.3	6.38-1.36	23.6	86	354
12	Landers	1992	Coolwater	strike-slip	7.3	1.42-0.61	19.7	82.1	271
13	Loma Prieta	1989	Capitola	strike-slip	6.9	0.85-1.49	15.2	9.8	289
14	Loma Prieta	1989	Gilroy Array #3	strike-slip	6.9	0.67-0.46	12.8	31.4	350
15	Manjil, Iran	1990	Abbar	strike-slip	7.4	2.16-0.82	12.6	40.4	724
16	Superstition Hills	1990	El Centro Imp. Cent	strike-slip	6.5	2.67-1.42	18.2	35.8	192
17	Superstition Hills	1987	Poe Road (temp)	strike-slip	6.5	2.45-0.46	11.2	11.2	208
18	Cape Mendocino	1992	Rio Dell Overpass FF	thrust	7.0	2.37-1.29	14.3	22.7	312

(*Continued*)

ID	event	year	station	fault type	M_w[a)]	T_g (s) Comp.1-2	distance (km)		$Vs30$(m/s^2)
							Clst.[b)]	Epi.[c)]	
19	Chi-Chi, Taiwan, China	1999	CHY101	thrust	7.6	0.47-3.4	10.0	32.0	259
20	Chi-Chi, Taiwan, China	1999	TCU045	thrust	7.6	4.88-0.48	26.0	77.5	705
21	San Fernando	1971	LA- Hollywood Stor	thrust	6.6	3.74-2.24	22.8	39.5	316
22	Friuli, Italy	1976	Tolmezzo	thrust	6.5	0.51-0.66	15.8	20.2	425

a) Moment magnitude; b) closest distance from the recording site to the ruptured area (if available); c) distance from the recording site to the epicenter

Nomenclature

The following symbols are used in this paper:

A_{PT} = cross-sectional area of post-tensioning strands;

a_{fs}/b_{fs} = link width ratio;

b_{fs} = link depth at the end;

b_{fs}/t_{fs} = width-to-thickness ratio of fuse link ends;

D_{max} = maximum spectral acceleration intensity associated with SDC D;

D_{min} = minimum spectral acceleration intensity associated with SDC D;

E_{PT} = PT modulus of elasticity;

f_{yfs} = yield strength of the fuse;

f_{yPT} = yield strength of the post-tensioning strand;

f_{PTi} = initial post-tensioning stress;

F_{PTi} = initial post-tensioning force;

f_{ufs} = fracturing strength of the fuse;

f_{UPT} = ultimate strength of the post-tensioning strand;

f_{50} = median IDA curve;

f_{16} = 16% fractile curve;

f_{84} = 84% fractile curve;

k = logarithmic slope of the hazard curve;

k_0 = real and positive constant of the prediction of the site seismicity;

K_{AB} = hardening stiffness;

K_{fs} = initial fuse stiffness;

K_{OA} = initial stiffness of the archetype;

K_X = standard normal value of the inverse cumulative distribution index of x;

L_{eff} = unbraced length of the brace;

L_{fs} = effective width of the fuse;

L_{fs}/t_{fs} = slenderness ratio;

L_{PT} = length of the post-tensioning strand;

M_{fsy} = yield moment of the fuse;

M_u = overturning moment;

M_{UP} = uplift moment of the system;

M_w = moment magnitudes;

M_y = yield moment of the system;

N_{fs} = number of fuses;

Nl_{fs} = number of links per fuse;

N_{PT} = number of post-tensioning strands;

P_D = total gravity load;

R = response modification coefficient;

S_a = spectral intensity at the fundamental period of the archetype;

SC = self-centering ratio;

S_{DS} = design, 5% damped spectral response acceleration parameter at short period;

S_{D1} = design, 5% damped spectral response acceleration parameter at a period of 1 s;

S_{MT} = spectra intensity at maximum considered earthquake ground motion;

$\hat{S}_{LS}$ = median limit state spectral intensity for the entire ground motion record set;

t = fundamental period of the system;

t_{fs} = plate thickness of the fuse;

V_{fp} = shear strength of the fuse;

V_{max} = maximum lateral strength;

V = design base shear of the system;

X = confidence level;

α = hardening ratio;

β = energy dissipation ratio;

$\beta_{C,U}$ = capacity uncertainty;

$\beta_{C,R}$ = capacity aleatory randomness;

$\beta_{EDP,R}$ = demand aleatory randomness;

$\beta_{EDP,R|16}$ = demand randomness calculated by 16% fractile;

$\beta_{EDP,R|84}$ = demand randomness calculated by 84% fractile;

$\beta_{EDP,R|s}$ = aleatory randomness of demand at each seismic intensity level;

β_{Des} = design requirement-related uncertainty;

β_{MDL} = model uncertainty;

$\beta_{total,D}$ = test data-related uncertainty;

β_{TOT} = total uncertainty;

$\beta_{total,R}$ = record to record uncertainty;

$\beta_{total,U}$ = total epistemic uncertainty;

β_{UD} = demand uncertainty;

δ_u = ultimate roof drift ratio;

δ_{up} = system uplift drift;

$\delta_{y,eff}$ = effective yield roof drift ratio;

δ_y = yield drift of the system;

ε_i = initial strain of the post-tensioning strand;

ε_{limit} = strain limit of the post-tensioning strand;

ε_m = fracture strain of the post-tensioning strand;

ε_{target} = target strain of the post-tensioning strand;

ε_u = ultimate strain of the post-tensioning strand;

ε_y = yield strain of the post-tensioning strand;

ϕ= capacity factor;

$\phi^{-1}(x)$ = inverse cumulative distribution function of the normal variable of x;

γ = demand factor;

γ_m = shear strain of the fuse;

λ^{LS} = mean annual frequency of exceeding a given limit-state;

λ^{P_0} = acceptable risk of occurring a limit state at a given seismic intensity;

λ_x = confidence factor.

References

1. American Society of Civil Engineers (ASCE). Seismic rehabilitation standards committee. Seismic rehabilitation of existing buildings. ASCE/SEI 41–10. Reston, VA, 2010
2. International building code. Int Code Counc Inc(formerly BOCA, ICBO SBCCI). IBC ICC, Falls Church, VA, 2006, 4051: 60478–65795
3. Wiebe L, Christopoulos C. Performance-based seismic design of controlled rocking steel braced frames. I: Methodological framework and design of base rocking joint. Journal of Structural Engineering, 2014, 141(9): 04014226
4. Ramirez C M, Miranda E. Significance of residual drifts in building earthquake loss estimation. Earthquake Engineering & Structural Dynamics, 2012, 41(11): 1477–1493
5. Iwashita K, Kimura H, Kasuga Y, Suzuki N. Shaking table test of a steel frame allowing uplift. J Struct Constr Eng, 2002, 1(561): 47–54
6. Ajrab J J, Pekcan G, Mander J B. Rocking wall-frame structures with supplemental tendon systems. Journal of Structural Engineering, 2004, 130(6): 895–903
7. Grigorian C, Grigorian M. Performance control and efficient design of rocking-wall moment frames. Journal of Structural Engineering, 2015, 142(2): 04015139
8. Buchanan A, Deam B, Fragiacomo M, Pampanin S, Palermo A. Multi-storey prestressed timber buildings in New Zealand. Structural Engineering International, 2008, 18(2): 166–173
9. Francesco S, Palermo A, Pampanin S. Quasi-static cyclic testing of two-thirds scale unbonded posttensioned rocking dissipative timber walls. Journal of Structural Engineering, 2015, 142(4): E4015005
10. Rojas P, Ricles J M, Sause R. Seismic performance of post-tensioned steel moment resisting frames with friction devices. Journal of Structural Engineering, 2005, 4(529): 529–540
11. Moradi S, Alam M, Milani A. Cyclic response sensitivity of post-tensioned steel connections using sequential fractional factorial design. J Struct Constr Eng, 2015, 112(1): 155–166
12. Toranzo L A, Restrepo J I, Mander J B, Carr A J. Shake-table tests of confined-masonry rocking walls with supplementary hysteretic damping. Journal of Earthquake Engineering, 2009, 13(6): 882–898
13. Eatherton M R, Hajjar J F. Large-scale cyclic and hybrid simulation testing and development of a controlled-rocking steel building system with replaceable fuses. Newmark Structural Engineering Laboratory. University of Illinois at Urbana-Champaign, 2010.
14. Ma X, Krawinkler H, Deierlein G. Seismic design and behavior of self-centering braced frame with controlled rocking and energy dissipating fuses. Blume earthquake Eng. Vol. 174. Center TR, University of Stanford, 2011
15. Latham D A, Reay A M, Pampanin S. Kilmore Street Medical Centre: Application of an Advanced Flag-Shape Steel Rocking System. In: Proceedings of the 2013 NZSEE Conf. Wellington, New Zealand, 2013
16. Roke D, Sause R, Ricles J M, Gonner N. Design concepts for damage-free seismic-resistant self-centering steel concentrically-braced frames. In: Proceedings of the 14th World Conf Earthq Eng. China, 2008
17. Clough R W, Huckelbridge A A. Preliminary experimental study of seismic uplift of a steel frame. Report No. UCB/EERC 77–22, Earthquake Engineering Research Center, College of Engineering, University of California, 1977
18. Kelly J M, Tsztoo D F. Earthquake simulation testing of a stepping frame with energy-absorbing devices. Report No. EERC 77–17, Earthquake Engineering Research Center, College of Engineering, University of California, 1977
19. Pollino M, Bruneau M. Seismic testing of a bridge steel truss pier designed for controlled rocking. Journal of Structural Engineering, 2010, 136(12): 1523–1532
20. Wiebe L, Christopoulos C, Tremblay R, Leclerc M. Mechanisms to limit higher mode effects in a controlled rocking steel frame. 1: Concept, modelling, and low-amplitude shake table testing. Earthquake Engineering & Structural Dynamics, 2013, 42(7): 1053–1068
21. Hosseini M, Fekri M, Yekrangnia M. Seismic performance of an innovative structural system having seesaw motion and columns equipped with friction dampers at base level. Structural Design of Tall and Special Buildings, 2016, 25(16): 842–865
22. Roke D, Sause R, Ricles J M, Seo C Y, Lee K S. Self-centering seismic-resistant steel concentrically braced frames. In: Proceedings of the 8th US National Conf Earthq Eng, San Francisco, USA, 2006
23. Sause R, Ricles J M, Roke D A, Chancellor N B, Gonner N P. Seismic performance of a self-centering rocking concentrically-braced frame. In: Proceedings of the 9th US and 10th Canadian Conf Earthq Eng. Toronto, Canada, 2010
24. Sause R, Ricles J M, Roke D, Seo C Y, Lee K S. Design of self-centering steel concentrically-braced frames. In: Proceedings of the 4th International Con Earthq Eng, Taipei, Taiwan, China, 2006
25. Chancellor N B, Akbas G, Sause R, Ricles J M, Tahmasebi E, Joó A L. Evaluation of performance-based design methodology for steel self-centering braced frame. San Francisco 7th International Conf on Behaviour of Steel Structures in Seismic Areas (STESSA 2012), Santiago, Chile, 2012
26. Eatherton M, Hajjar J F, Deierlein G, Krawinkler H, Billington S, Ma X. Controlled rocking of steel-framed buildings with replaceable

energy-dissipating fuses. In: Proceedings of the 14th World Conf Earthq Eng. Beijing, China, 2008.
27. Wiebe L, Christopoulos C. Mitigation of higher mode effects in base-rocking systems by using multiple rocking sections. Journal of Earthquake Engineering, 2009, 13(SP1): 83–108
28. Mar D. Design examples using mode shaping spines for frame and wall buildings. In: Proceedings of the 9th US and 10th Canadian Conf Earth Eng. Toronto, Canada, 2010
29. Rahgozar N, Moghadam A S, Aziminejad A. Quantification of seismic performance factors for self-centering controlled rocking special concentrically braced frame. Structural Design of Tall and Special Buildings, 2016, 25(14): 700–723
30. Tahmasebi E, Sause R, Ricles J M, Chancellor N B, Akbas T. Probabilistic Collapse Performance Assessment of Self-Centering Concentrically Braced Frames. In: Proceedings of the 10th US Natl Conf Earthq Eng. Anchorage, AK, USA, 2014
31. Ahmadi O, Ricles J M, Sause R. Seismic collapse resistance of self-centering steel moment resisting frame systems. Proc. 10th US Natl. Conf. Earthq. Eng. Anchorage, AK, USA, 2014
32. Lin L, Naumoski N, Foo S, Saatcioglu M. Probabilistic assessment of the seismic vulnerability of reinforced concrete frame buildings in Canada. In: Proceedings of the 14th world conference on earthquake engineering. Beijing, China, 2008
33. Venture S A C J, Committee G D, Venture S A C J. Recommended seismic design criteria for new steel moment-frame buildings. Federal Emergency Management Agency. Report No. FEMA-350, 2000
34. Jalayer F. Direct probabilistic seismic analysis: implementing non-linear dynamic assessments. Stanford University, 2003
35. Vamvatsikos D. Derivation of new SAC/FEMA performance evaluation solutions with second-order hazard approximation. Earthquake Engineering & Structural Dynamics, 2013, 42(8): 1171–1188
36. Jalayer F, Cornell C A. A technical framework for probability-based demand and capacity factor (DCFD) seismic formats. RMS, 2003
37. Baker J W, Cornell C A. Uncertainty specification and propagation for loss estimation using FOSM method. Pacific Earthquake Engineering Research Center, College of Engineering, University of California, 2003
38. Yun S Y, Hamburger R O, Cornell C A, Foutch D A. Seismic performance evaluation for steel moment frames. Journal of Structural Engineering, 2002, 128(4): 534–545
39. Luco N. Probabilistic seismic demand analysis, SMRF connection fractures, and near-source effects. Stanford University, 2002
40. Eatherton M R, Ma X, Krawinkler H, Mar D, Billington S, Hajjar J F, Deierlein G G. Design concepts for controlled rocking of self-centering steel-braced frames. Journal of Structural Engineering, 2014, 140(11): 195–203
41. Ma X, Borchers E, Pena A, Krawinkler H, Deierlein G. Design and behavior of steel shear plates with openings as energy-dissipating fuses. John A. Blume Earthquake Engineering Center Technical Report, 2010
42. Mazzoni S, McKenna F, Scott M H, Fenves G L. OpenSees command language manual. Pacific Earthq Eng Res (PEER) Cent, 2006
43. Liu J, Astaneh-Asl A. Moment-rotation parameters for composite shear tab connections. Journal of Structural Engineering, 2004, 130 (9): 1371–1380
44. Applied Technology Council for the Federal Emergency Management Agency. Quantification of Building Seismic Performance Factors. Report no. FEMA P695. Redwood, CA, 2009
45. Vamvatsikos D, Cornell C A. Incremental dynamic analysis. Earthquake Engineering & Structural Dynamics, 2002, 31(3): 491–514
46. Haselton C B. Assessing seismic collapse safety of modern reinforced concrete frame buildings. Dissertation for the Doctoral Degree, Stanford, California: Stanford University, 2006
47. Ibarra L F, Krawinkler H. Global collapse of frame structures under seismic excitations. Report No. 152, John A. Blume Earthquake Engineering Center, Dept. of Civil and Environmental Engineering, Stanford University, Stanford, California, USA, 2005
48. Gogus A, Wallace J W. Seismic safety evaluation of reinforced concrete walls through FEMA P695 methodology. Journal of Structural Engineering, 2015, 141(10): 4015002
49. Lee T H, Mosalam K M. Seismic demand sensitivity of reinforced concrete shear-wall building using FOSM method. Earthquake Engineering & Structural Dynamics, 2005, 34(14): 1719–1736
50. Baker J W, Cornell C A. Uncertainty propagation in probabilistic seismic loss estimation. Structural Safety, 2008, 30(3): 236–252
51. Liel A B, Haselton C B, Deierlein G G, Baker J W. Incorporating modeling uncertainties in the assessment of seismic collapse risk of buildings. Structural Safety, 2009, 31(2): 197–211
52. Ibarra L, Krawinkler H. Variance of collapse capacity of SDOF systems under earthquake excitations. Earthquake Engineering & Structural Dynamics, 2011, 40(12): 1299–1314
53. Baker J W. Efficient analytical fragility function fitting using dynamic structural analysis. Earthquake Spectra, 2015, 31(1): 579–599